Review

Compact, Wearable Antennas for Battery-Less Systems Exploiting Fabrics and Magneto-Dielectric Materials

Alessandra Costanzo [1,*]**, Diego Masotti** [2] **and Martino Aldrigo** [3]

[1] DEI, University of Bologna, via Venezia 52, 47152 Cesena, Italy

[2] DEI, University of Bologna, viale Risorgimento 2, 40136 Bologna, Italy;
    E-Mail: diego.masotti@unibo.it

[3] MIMOMEMS, IMT, 077190 Bucharest, Romania; E-Mail: martino.aldrigo@imt.ro

* Author to whom correspondence should be addressed; E-Mail: alessandra.costanzo@unibo.it;
    Tel.: +39-51-2093059; Fax: + 39-51-2093053.

Abstract: In this paper, we describe some promising solutions to the modern need for wearable, energy-aware, miniaturized, wireless systems, whose typical envisaged application is a body area network (BAN). To reach this goal, novel materials are adopted, such as fabrics, in place of standard substrates and metallizations, which require a systematic procedure for their electromagnetic characterization. Indeed, the design of such sub-systems represents a big issue, since approximate approaches could result in strong deviations from the actual system performance. To face this problem, we demonstrate our design procedure, which is based on the concurrent use of electromagnetic software tools and nonlinear circuit-level techniques, able to simultaneously predict the actual system behavior of an antenna system, consisting of the radiating and of the nonlinear blocks, at the component level. This approach is demonstrated for the design of a fully-wearable tri-band rectifying antenna (rectenna) and of a button-shaped, electrically-small antenna deploying a novel magneto-dielectric substrate. Simulations are supported by measurements, both in terms of antenna port parameters and far-field results.

---

1. Introduction

Nowadays, there is an increasing demand for the miniaturization of all modern transceiver components, mainly due to the need for combining their computational capabilities and portability: one of the main design constraints becomes their integration in small volumes (on the order of some cm^3 or even less).

A big push to distributed and pervasive wireless systems applications is also given by the so-called body area networks (BANs), where small and ultra-low-power sensors create a wireless network with a coverage limited to the space surrounding the human body.

These technological trends put into evidence the necessity to contemporaneously fulfill different and conflicting needs: in spite of the small volume of the possibly wearable sensor, its energy consumption should be low, and in modern low-environmental impact engineering applications, its energy autonomy is envisaged.

In this scenario, a strategic role is played by the accurate design capability of innovative wireless devices to be deployed in wearable [1] and, in perspective, implantable BANs. Due to the typically small power budget involved, to the presence of non-conventional wireless links and innovative materials, the optimization of this family of radiating sub-systems is a delicate issue: the rigorous electromagnetic (EM) description of the whole scenario is mandatory in order to achieve reliable results. The unavoidable presence of nonlinear devices forces a circuit-level layout-wise nonlinear/EM design approach [2].

In this paper, we first focus the attention on the need for accurately characterizing from the EM point of view the innovative materials adopted in the design process [3–5]. We then describe our computer aided design (CAD) platform based on the concurrent exploitation of nonlinear and EM analyses, representing an indispensable tool for the design of wearable radio frequency (RF) energy harvesters [6]. This multi-domain CAD approach is applied to the accurate design of a highly efficient, completely wearable, tri-band rectifying antenna (rectenna), consisting of a compact multilayer structure resonating at the GSM 900, GSM 1800 and WiFi frequencies [7,8]. Since the most space-consuming component in modern transceivers is the radiating element, to ensure the best radiation efficiency, we finally describe the promising design of an electrically small UHF antenna built on an innovative magneto-dielectric (MD) material: the EM properties of the adopted hexaferrite substrate can be efficiently exploited for miniaturization purposes by planar patch topologies, as demonstrated by the proposed button-shaped solution [9].

In both the described projects, prototype realization and wide measurement campaigns are presented to demonstrate the accuracy of the design procedure.

2. Wearable Material Characterization

The wearable characteristic/feature of radiating systems has been pursued by resorting to truly wearable materials or by achieving a miniaturization of the antenna itself through the exploitation of dense material from both the dielectric and the magnetic constitutive characteristics. In both cases, an accurate electromagnetic characterization of material properties is needed to carry out a successful design of the radiating systems under exam.

There is a wide plethora of textile substrates, some of them EM-characterized for wearable applications [10,11], even if not always extensively from the frequency band point of view. Significant effort has also been done to study the effects of adverse conditions in wearable antenna applications [11–14].

For our first design, we select a common pile fabric to be used as the substrate of a planar antenna, adopting a metallic fabric for the conductive parts of the system. This materials' combination allows a fully-flexible system to be completely integrated, or even hidden, in garments. As an alternative solution, we have studied a new magneto-dielectric material allowing efficient antenna realization in the UHF band with dimensions comparable to garment buttons. The information on material properties is totally missing in these cases. To define the relative permittivity ε_r and dielectric loss tangent $\tan\delta_\varepsilon$ of the fabrics, analytical methods based on structure can be adopted [3,4], as described in the following. Measurements of the same resonant structures can be used for controlling the analytical results.

A more complex situation has to be faced for the complete characterization of a magneto-dielectric substrate, since two further unknowns need be defined, namely the relative permeability μ_r and the magnetic loss tangent $\tan\delta_\mu$. In this case, a reverse model engineering approach is chosen and the material characteristics are derived by a set of measured scattering parameters of a two-port planar resonant structure.

Let us consider firstly the simpler case of the non-conductive 4 mm-thick pile fabric (labelled Pile 1), used as the dielectric support for the wearable antenna described in Section 3. The procedure we adopt for the EM-characterization of the material consists of the following steps: (I) we start from an estimation of the relative permittivity and the design of a T-resonator based on this estimation; (II) using full-wave solvers [15], a large database containing the scattering parameters of the resonator is built by varying the EM-properties of the substrate (ε_r and $\tan\delta_\varepsilon$); (III) then, the same resonator is realized on a pile substrate (see Figure 1a) and the transmission coefficient between Port 1 and Port 2 (S_{21}) is measured up to 3 GHz with a network analyzer Agilent N1996A; the prototype EM characteristics are derived from the S-parameters measurements, both using [3] and by comparison with the EM-database. In the present case, the identical resulting relative permittivity and loss tangent values provided by the two approaches are 1.23 and 0.0019, respectively.

Figure 1. (**a**) Photo of the wearable T-resonator prototype. (**b**) Measured and simulated transmission coefficient behavior *vs.* frequency.

(a)							(b)
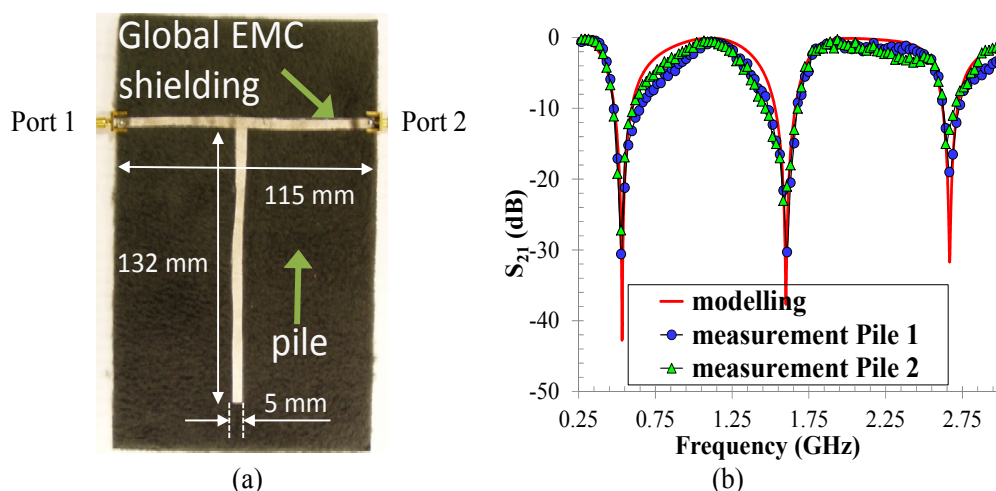
This is demonstrated in Figure 1b, where an excellent correspondence between the measured transmission coefficient S_{21} and the corresponding best-fitted simulated result (obtained with $\varepsilon_r = 1.23$ and $\tan\delta_\varepsilon = 0.0019$) is clearly demonstrated. Since various sorts of pile fabrics, considerably different from the sight and touch points of view, were provided by the same vendor, we also realize a second identical T-resonator on a second pile sample (labelled Pile 2), whose transmission coefficient is superimposed on the same figure: fortunately, almost identical EM properties pertain to this sample, too, since excellent correspondence with the EM-simulated behavior is again achieved.

As regards the conductive fabrics, there are two alternatives: (I) conductive threads, created from single or multiple strands of conductive and nonconductive fibers; (II) electro-textiles, mostly created by incorporating conductive threads into fabrics by means of weaving and knitting. We resort to the second solution, in particular to the Global EMC shielding fabric as the conductive material. This choice is due to several reasons: the low surface resistivity (0.02 Ω/sq) of this material, its minimal fraying with respect to other fabrics, which allows precise and accurate cuts/slots, and the robustness of its thermo-adhesion to the pile substrate.

The situation is more complex in the presence of a material with both permittivity and permeability greater than one. The unknowns to be estimated are four in this case ($\varepsilon_r = \varepsilon' - j\varepsilon''$, $\tan\delta_\varepsilon = \varepsilon''/\varepsilon'$, $\mu_r = \mu' - j\mu''$, $\tan\delta_\mu = \mu''/\mu'$), and the theory of the quasi-transverse EM (Q-TEM) microstrip mode exploited in [3,4] is not present in the literature, to the authors' knowledge, and is currently under development. Due to the lack of knowledge of the complex characteristic variability range, the EM-based numerical approach previously adopted would have been too time-consuming in this case. For this reason, we resort to direct measurements of material samples by means of an Agilent E4991A RF Impedance/Material Analyzer in the band 1 MHz–3 GHz [9]. Table 1 reports the results of the measured parameters extraction and the corresponding best fitting with the EM tool Lorentz dispersive model [15] of the hexaferrite sample at our disposal: at the frequency of 868 MHz, where the design of the miniaturized patch antenna described in Section 4 is carried out, the adopted material exhibits a value of $\varepsilon' \approx 12$ and a value of $\mu' \approx 2$, with a dielectric loss tangent $\varepsilon''/\varepsilon' \approx 0.01$ and a magnetic loss tangent $\mu''/\mu' \approx 0.38$. This results in a refraction index of approximately five.

Table 1. Measured and modelled values of the complex permittivity and permeability of the hexaferrite sample in the frequency band of interest.

Freq.	ε'		ε''		μ'		μ''	
	Measured	Modelled	Measured	Modelled	Measured	Modelled	Measured	Modelled
750 MHz	12.231	12.230	0.112	0.103	2.044	2.063	0.771	0.713
868 MHz	12.277	12.283	0.131	0.141	2.072	1.961	0.798	0.747
1 GHz	12.339	12.346	0.194	0.194	2.200	1.856	0.774	0.766

3. Design of a Wearable Multi-Layer Multi-Resonant Rectenna

Recent technology trends in ultra-low power microcontrollers and sensors pave the way to applications requiring small amounts of power (from a few μW to a few hundreds of μW). For this purpose, ubiquitously available radio frequency (RF) sources, operating at different bands, with unknown directions of incidence and polarizations, can be exploited by rectifying antenna (rectenna) systems to provide a solution to this problem [16,17]. However the available amount of RF energy is

low, even in highly humanized environments [18], and typically, only a few µW of power can be provided by highly efficient rectennas. We thus imagine that these systems could be more suitable for "RF upon request" applications [19], always exploiting the sources typically present in all humanized environments, but in correspondence with a precise demand by the user (e.g., a nearby mobile phone call). From this point of view, a fully-wearable rectenna for technology garments can find its proper application [7,20]. The design of such a system is a delicate issue, since there is a number of challenging aspects in RF energy harvesting to be considered, such as the spatial/temporal variability of RF sources and the frequency of operation: thus, a useful rectenna must have a highly efficient antenna, operating at different bands, with unknown direction of incidence of the incoming field, and must efficiently rectify the received RF power. When wearable devices are concerned, additional problems have to be faced: the effects of body and of topology variation (e.g., layer bending and/or shift) on the system performance must be accounted for.

Here, we describe the accurate design of a highly efficient, completely wearable tri-band rectenna, consisting of a compact multilayer structure resonating at the GSM 900, GSM 1800 and WiFi frequencies.

3.1. Design Procedure

The different design domains, firstly introduced in [6], that should be adopted to accurately define and dimension the building blocks of a harvesting system are schematically depicted in Figure 2. Note that in this formulation, the RF harvesting system is expected to operate whenever the RF energy is available and to store it for immediate or future usage in an efficient way, through a power management unit. Thus, the operating rates of the entire system spans from the microwave spectrum, where the RF energy is located, down to the baseband, where the DC/DC converter operates.

Figure 2. Block diagram of the multi-domain CAD tool for rectenna design.
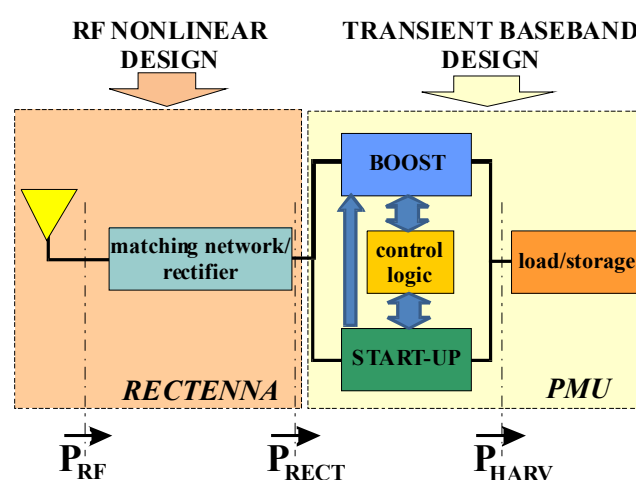
The key difficulty for this class of systems design is thus the ability to combine the results of the nonlinear rectenna regime, more suitable for the harmonic-balance analysis based on complex phasors, with the time-domain results needed for the correct dimensioning of the DC/DC converter. The correct combinations of these domains is of fundamental importance, to correctly account for the impedances of the different sub-blocks.

At RF, the subsystem consisting of the receiving antenna, loaded by the rectifier, and of the antenna-rectifier inter-stage network needs to be designed in a steady-state nonlinear regime by means of electromagnetic theory and software tools typical of an RF design environment, such as Harmonic Balance (HB). At this stage, the network function to be optimized is the RF-to-DC conversion efficiency, given by:

$$\eta_{RF-DC} = \frac{P_{RECT}}{P_{AV}} \tag{1}$$

where P_{AV} is the available RF energy on the antenna location, while P_{RECT} is the rectified power at the rectenna output port, delivered to a fixed optimum load.

At baseband, the transient design of a DC-DC converter, keeping the rectifier dynamically close to the optimum load condition, is designed by transient analysis: the efficiency to be maximized in this case is a DC-to-DC efficiency, given by [6]:

$$\eta_{DC-DC} = \frac{F\,E_{HARV}}{P_{RECT}\,T_C} = \frac{P_{HARV}}{P_{RECT}} \tag{2}$$

as the ratio between a fraction ($F < 1$, ~90%) of the maximum energy stored in the output storage capacitor (E_{HARV}) during its charging time T_C.

For the RF nonlinear design, we refer to the situation depicted in Figure 3a, where the wearable rectenna is immersed in a multi-source environment. For any given RF source at an angular frequency ω_{RF}, we resort to EM theory [21,22] to effectively estimate the actual RF power available to the rectifier circuit (P_{AV} in Equation (1)). Under the assumption of "plane-wave approximation" for the incoming RF field ($\mathbf{E}_i$ of Figure 3b), which normally holds for conventional communication systems, the Norton equivalent current source can be easily cast in the following way [6]:

$$J_{eq}\left(\omega_{RF}\right) = j\,\frac{\left[1 + R_0 Y_H(\omega_{RF})\right]}{U}\,\frac{2\lambda_{RF}\,re^{j\beta r}}{\eta}\,\mathbf{E}_i(\mathrm{r};\omega_{RF}) \bullet \mathbf{E}_H\left(\mathrm{r};\omega_{RF}\right) \tag{3}$$

where $\mathbf{E}_H$ is the far-field vector at the same RF frequency radiated by the harvesting antenna (described by the EM-based admittance Y_H), when operating in the transmitting mode, powered by a voltage source of known amplitude U and internal resistance R_0. Here, r is the spatial vector defining the RF source direction of arrival in the receiver-referred spherical reference frame. It is worth noting that in the case of harvesting upon-request, the link between the RF source (e.g., mobile phone) and the receiving harvester antenna can be "unconventional": it means that the "plane-wave approximation" may not be valid any more, due to the far-field condition violation and/or the exploitation of a link direction different from the maximum one. Furthermore, in this case, the equivalent current generator can be obtained in a rigorous way, resorting to Love's equivalence principle [23], according to the following formula:

$$J_{eq}(\omega_{RF}) = \frac{1 + R_0 Y_H(\omega)}{U} \bullet \quad \hat{\mathbf{n}} \bullet \int_{\Sigma} \left[\mathbf{E}_i(P_\Sigma) \times \mathbf{H}_H(P_\Sigma) - \mathbf{E}_H(P_\Sigma) \times \mathbf{H}_i(P_\Sigma)\right] d\Sigma \tag{4}$$

where the electric and magnetic fields of both the RF source and the harvester antenna are numerically evaluated on a Σ plane placed in between the two antennas. Formula (4) provides correct results

irrespective of the antenna orientations and transmitter-to-harvester distance and eventually takes into account the nearby objects affecting the link (such as the human body in Figure 3b) [6].

Note that by means of Equation (3) or Equation (4), polarization mismatch between the rectenna and the incident field is automatically and rigorously taken into account.

Figure 3. (**a**) Wearable rectenna in the presence of multiple incident RF sources. (**b**) Electromagnetic (EM) representation of the sources as EM fields interacting with the harvesting antenna (to be used in the evaluation of Equations (3) and (4)). (**c**) Circuit-level equivalent description of the tri-band wearable rectenna.
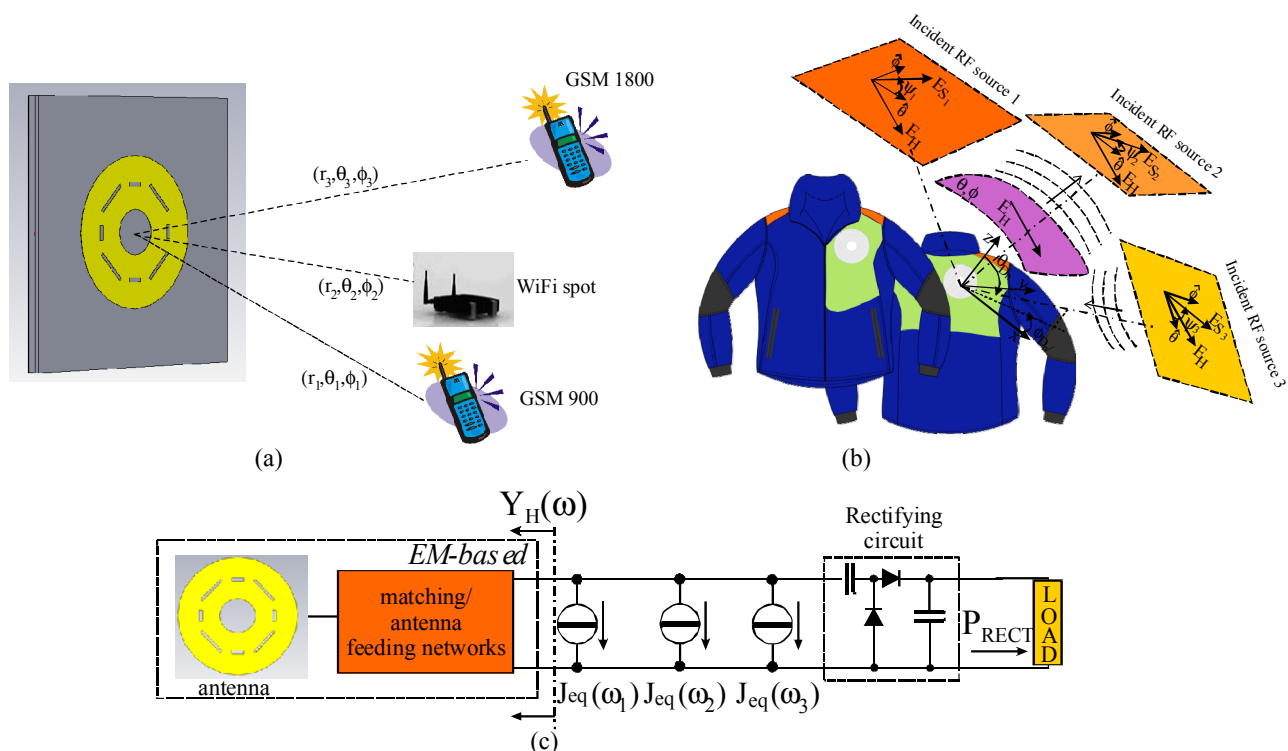

By resorting to the circuit-level description of Figure 3c, a straightforward nonlinear HB optimization can be easily performed, contemporaneously focusing on the frequency bands of interest. Moreover, the rectenna nonlinear regime due to the simultaneous incidence of multiple ambient RF sources is directly provided by a multi-tone HB analysis (as in the case to which Figure 3c refers).

In the present design, we focus on the two GSM and WiFi frequency bands (900 MHz, 1,800 MHz and 2,450 MHz, respectively). Our architecture choice consists of a single multi-resonant antenna with a single rectifying section: this way, the unwanted EM-couplings always present in multi-antenna solutions are avoided, as well as the minimization of diode losses is achieved. The final engineered solution of the present rectenna is shown in Figure 4, where the multi-layer adopted layout is also evident [7].

Besides the pile substrate for the antenna, another grounded pile layer is adopted for better isolation of the human body. The only non-wearable portion is the yellow portion of Figure 4, consisting of the 0.1 mm-thick flexible Kapton substrate ($\varepsilon_r = 3.4$, $\tan\delta_\varepsilon = 0.002$) under the ground plane. Its area is reduced to a minimum in order to guarantee a more comfortable wearable solution: it only contains the antenna feeding network (matching network, phase shifter and power divider) and the rectifier circuit.

Figure 4. Stack-up of the proposed tri-band wearable rectenna.
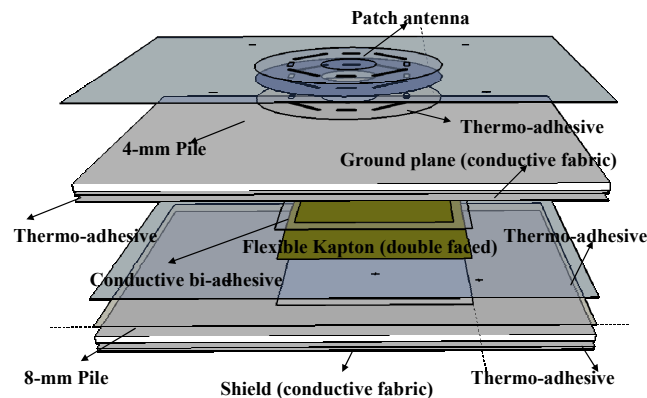
The use of a single tri-band antenna, instead of a broadband one, represents the best choice in the case of low available power budgets, since the resonant behavior at each frequency is a synonym of high antenna efficiency, a fundamental requisite for the maximization of P_{RF}. In this case, we adopt an annular ring planar antenna for the exploitation of higher order modes, such as the TM12, having superior radiation properties [24]. In Figure 5a, the theoretical current distribution for the three selected modes (TM11, TM21 and TM12) is reported for a generic annular patch. The main difficulty is to exactly match the three desired frequencies to the three selected modes: this is impossible by only acting on inner and outer radii dimensions; for this reason, we etch eight symmetric slots in the conductive fabric of the patch and use their dimensions as tuning parameters, thus achieving the following desired correspondence of the modes resonance frequencies: TM11 at 900 MHz, TM21 at 1,800 MHz, and TM12 at 2,450 MHz [8]. Figure 5c shows the final slotted annular ring topology, with inner and outer radii of 21 and 71 mm, respectively, obtained after a sequence of parametric full-wave analyses for different slot area values; while in Figure 5b, the modelled surface currents at the three resonances are reported. In spite of the slotted surface, the current distribution is quite similar to the theoretical one.

Figure 5. (**a**) Theoretical and (**b**) simulated electric current patterns for the ring antenna selected modes. (**c**) Final layout of the tri-band annular ring antenna.
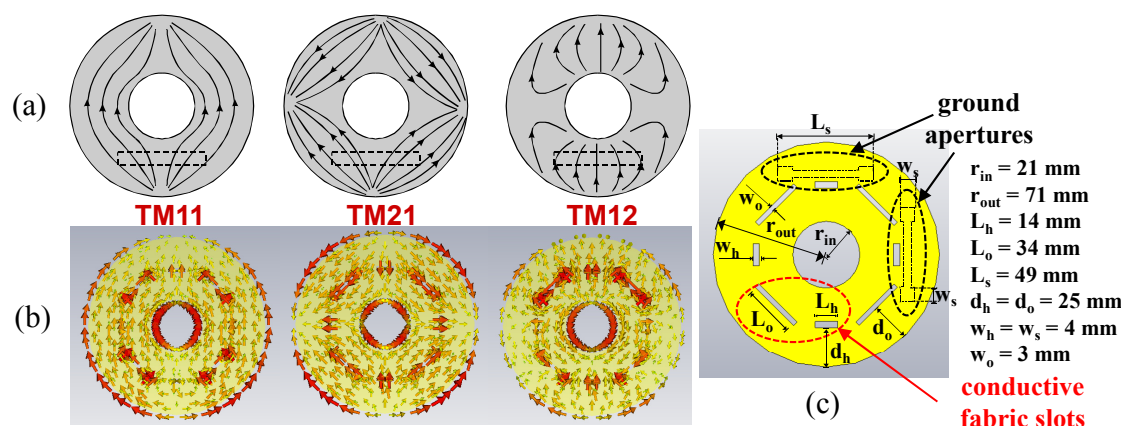
Another delicate issue is the shape and position of the coupling slot in the ground plane used for antenna excitation (the dashed shape in Figure 5c). Two coupling slots are needed for the circular

polarization purposes of the two-ports harvesting antenna, and the best tradeoff between good port matching and low port decoupling is obtained with a "dog bone" shape [7].

The multi-band linear feeding network design is first carried out at the circuit level, then layout-wise by means of a fine-tuning EM analysis. In both cases, the actual load offered by the antenna is taken into account: the resulting three-port network on a flexible Kapton layer (see Figure 6b) consists of a broadband 90° phase shifter (for circular polarization purposes) and a power divider. The matching network topology (an impedance step, in this case) is obtained as the final result of the multi-band HB nonlinear optimization (see Section 3.2).

The final layout of the multi-layered prototype is shown in Figure 6a. Due to the placement of the antenna on a jacket (Figure 3b), there is enough space for a large antenna ground plane: this improves the antenna directivity and reduces the human body effects.

Figure 6. (**a**) Photo of the multi-layered rectenna prototype. (**b**) Layout of the three-port feeding network; Port 1 is in DC, while Port 2 and Port 3 are the RF antenna feeding ports needed for ensuring circular polarization.

(a)   (b)
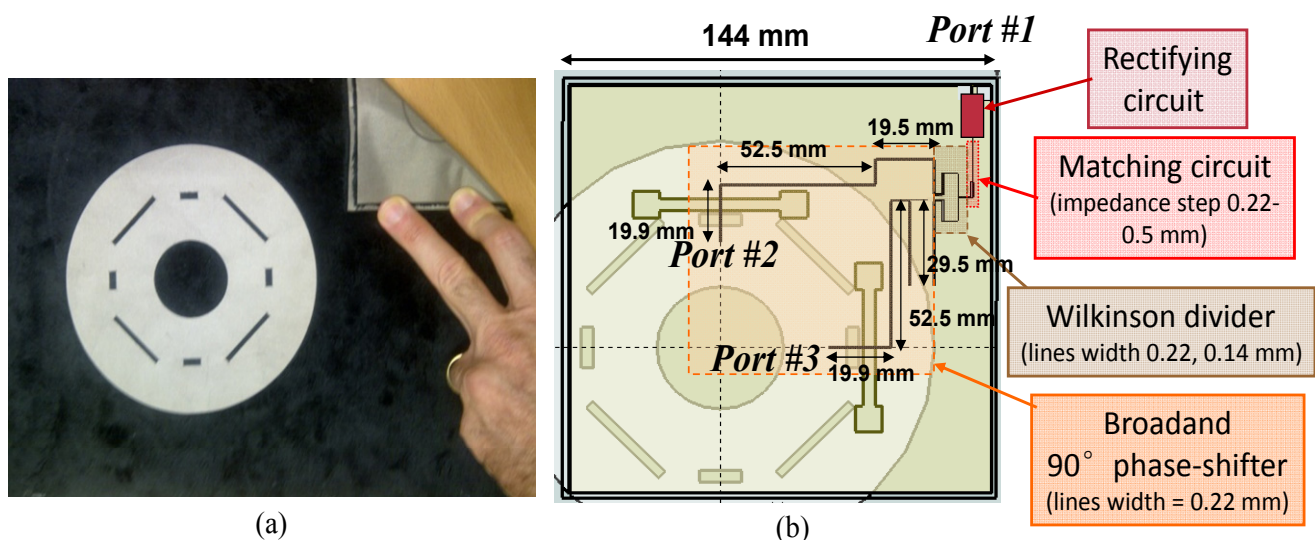
3.2. Results

The performance of the two-port antenna in terms of scattering parameter behavior and radiation patterns at all of the frequency bands of interest are given in Figures 7a,b and 8, respectively. A satisfactory agreement between measurements and simulations is obtained in both cases. A notable discrepancy occurs in terms of the reflection coefficient at 900 MHz: the sharpness of the corresponding resonance makes it the most delicate operating bandwidth, highly sensible to mechanical tolerances in ground aperture shape. The simulation of the two-port antenna with in-quadrature port excitation and a background plane area of 25×25 cm^2 provides efficiencies of 61%, 54% and 85% in ascending frequency order and realized gains equal to 4.7, 4.9 and 9.1 dB, respectively. An axial ratio less than 3 dB is obtained for the TM11 and TM12 mode for a wide elevation range; the TM21 mode is unable to provide circular polarization due to the exact superposition of the excited orthogonal modes (see Figure 5a).

Figure 7. (**a**) Measured and simulated reflection coefficient of the two-port ring antenna and simulated reflection coefficient dependence on pile-Kapton substrate misalignment. (**b**) Measured and simulated transmission coefficient of the two-port ring antenna.

(a)

(b)
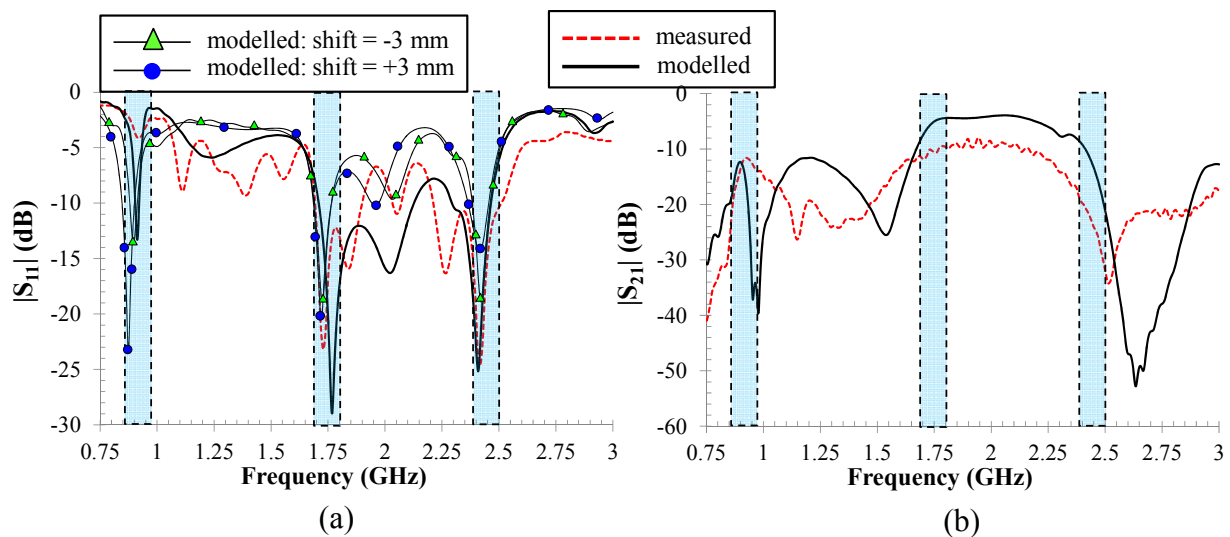
Figure 8. Measured and simulated radiation patterns of the two-port ring antenna at the three operating frequencies.
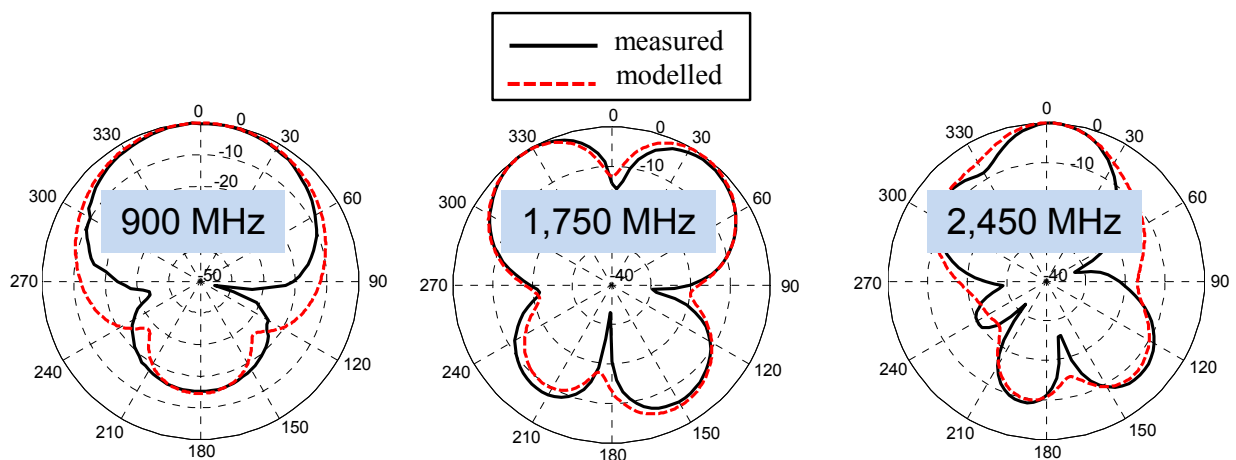

Figure 7a also reports the effects of an unpredictable, but probable, misalignment between the antenna and the Kapton layers. This could happen during the manual attaching procedure, despite suitable markers realized on the layers: a ±3 mm shift is the over-estimated range of uncertainty. The modeled scattering parameters shown in the figure guarantee a sufficient robustness of the rectenna design with respect to unwanted asymmetries: the maximum resulting shift is about 4% for the lower frequency, which is the most susceptible band, as measurements have demonstrated.

Two further simulations are carried out addressing bending and human body effects. Firstly, the antenna and the feeding layers are bent around a vacuum cylinder with a 150-mm diameter, corresponding to a typical adult chest. No significant variations with respect to the flat configuration are observed, provided that no misalignment occurs. Secondly, the cylinder is filled with a human-body-like material ($\varepsilon_r = 53.3$ and $\sigma = 1.52$ S/m); the presence of the 25×25 cm^2 back shielding fabric guarantees almost unchanged behavior, in this case, too.

Finally, a multi-band nonlinear optimization of the whole rectenna is carried out by the HB technique: design specifications are simultaneously given in terms of RF-to-DC conversion efficiency, at the three fundamental frequencies, by combining the frequency-dependent EM description of the antenna/phase-shifter with the nonlinear rectifying circuit. The latter consists of a single-stage, full-wave peak-to-peak RF-DC converter, as shown in Figure 3c: this simple rectifier topology, employing low-threshold-voltage diodes (Skyworks SMS7630), minimizes diode losses and represents the best choice for ultra-low-power applications [6,25]. At this stage, the design parameters are provided by the matching network layout: in this case, it simply consists of a microstrip impedance step. The power levels pertaining to the equivalent current generator Equation (3) (or Equation (4)):

$$P_{AV}(\omega_{RF}) = \frac{|J_{eq}(\omega_{RF})|^2}{8\,\mathrm{Re}[Y_H(\omega_{RF})]} \tag{5}$$

span the low-power range typical of scavenging scenarios (from few to few hundreds of µW), with ω_{RF} equal to 900, 1,800 and 2,450 MHz for the three bands application under exam.

Figure 9a finally provides the rectenna performance in terms of RF-to-DC conversion efficiency for the three operating frequencies, as a function of the power transmitted by a resonant dipole placed 30 cm away and in the maximum link direction. For the sake of clarity, the same figure also shows the corresponding RF available power abscissa axes: they obviously put into evidence the strong channel dependence on the operating frequency. Due to the adopted link distance, the field radiated by the dipole cannot be considered a uniform plane wave in the harvester location: for this reason, we resort to Equation (4) in the evaluation of Equation (5). The same figure reports also a good comparison with available measurements carried out in a real office scenario for typical low incident power levels. In more complex scenarios (*i.e.*, non-line-of-sight links), the inclusion in the CAD tool of the channel description is mandatory in order to obtain realistic predictions [26].

Figure 9. (**a**) Conversion efficiencies of the whole wearable rectenna at the three operating frequencies. (**b**) Rectified output voltage at the three operating frequencies and in the contemporaneous presence of the three tones.
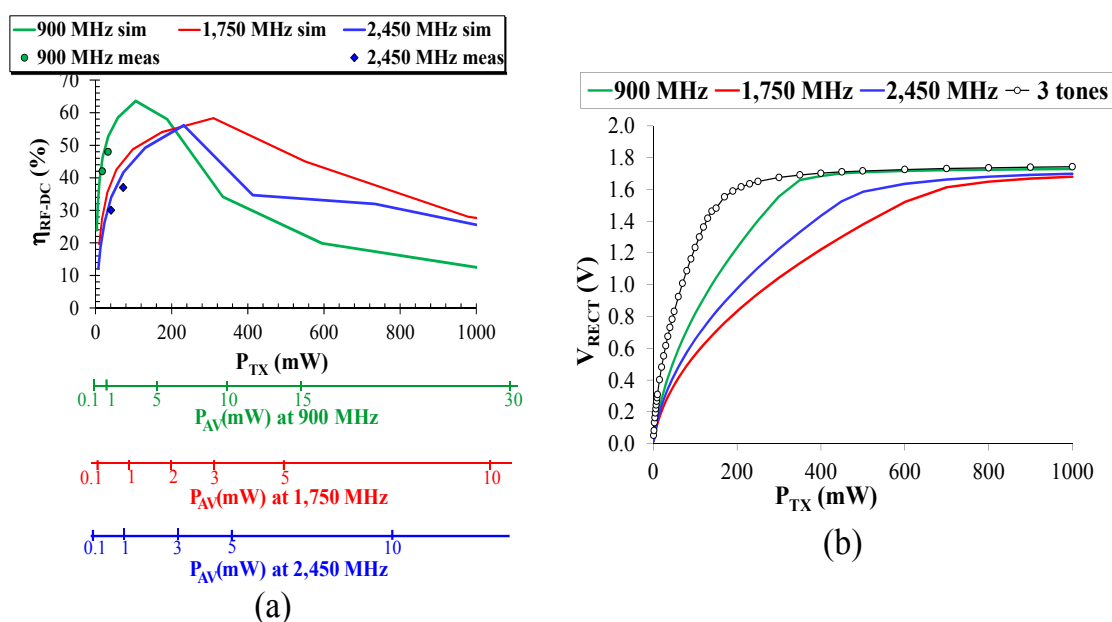
The presented procedure allows us to simultaneously account for the presence of various RF sources by means of a nonlinear multi-tone HB analysis (as envisaged in Figure 3), where the different tones are represented as independent rectenna excitations: intermodulation products up to the third order are considered in the HB simulation. In Figure 9b, the rectenna output DC voltages resulting from the superposition of different sources (solid line) and from single sources are compared, again as a function of the incident transmitted power. The transmitted power values of the figure are associated with one excitation in the single-tone analysis and are equally distributed across the different tones in the multi-tone case. It is worth noting that, at low power levels, the deployment of the intermodulation products generated by the nonlinearities improves the rectenna conversion capabilities. At higher levels, this effect is negligible.

4. Wearable Miniaturized Magneto-Dielectric Patch Antenna

The use of wearable or implantable radiating subsystems for body area networks applications has provided growing interest in the miniaturization of the most space-consuming component: the antenna. Many patch antenna miniaturization techniques have been proposed in the literature [27,28], but the corresponding reduction factor is unable to fulfill wearable/implantable applications. The main problem of this research field, which is still an open issue, is the unavoidable reduction of the radiation properties by exploiting electrically small antennas. Chip antennas on electrically dense ceramic materials (ε_r high) verify this assumption. Moreover, patch antennas on high-permittivity materials badly exploit the reduction factor provided by the reduced "guided wavelength" value ($\lambda_g = \lambda_0/\sqrt{\varepsilon_r}$). This is due to the fact that antennas whose radiation behavior relies on equivalent magnetic currents (as the case of patch antennas) do not take advantage of an increased value of the permittivity. Conversely, an increased value of the permeability can be positively exploited by patch antennas [29].

Starting from these assumptions we adopt an M-type barium-strontium hexaferrite $Ba_{0.75}Sr_{0.25}Fe_{12}O_{19}$ [30] for miniaturizing a patch antenna operating at 868 MHz [9]. The most significant advantage in using this kind of magnetic material as an antenna substrate is the high value of its ferro-magnetic resonance (FMR) (above 10 GHz, for the adopted sample): we can thus assume that our operating frequency band is sufficiently far from FMR and that the material properties are far from varying strongly and rapidly. This has been verified by the measurements reported in Table 1.

4.1. Antenna Design

The choice of antenna operating frequency is due to a wide deployment of the 868 MHz frequency for UHF-RFID applications in Europe. The sample of magneto-dielectric (MD) material we use has a disk shape without sharp edges, more suitable for wearable applications. Besides the consistent dimension reduction due to the high value of the material refractive index, we make also use of a standard antenna miniaturization technique: the use of a shorting plate [31], *i.e.*, an electric conductor wall directly connecting the antenna upper metallization to the ground plane allows us to halve the antenna length, thus reducing it to $\lambda_g/4$. Since the free-space wavelength is about 345 mm at 868 MHz, and the MD material refractive index is about the, the antenna's final length is ≈18 mm: this corresponds to a $\lambda_0/20$ antenna. The disk diameter is thus 33 mm, in order to allow enough space

between the radiating edge of the patch (the non-short circuited one) and the end of the disk. This way, an electrically small button-shaped antenna is obtained.

The use of the shorting mechanism suggests adopting the so-called planar inverted F-antenna (PIFA) architecture [31], employing a coaxial cable as the feeding solution. Two problems arise from previous technological choices: (I) the need to create a hole for the inner conductor of the coaxial cable inside the fragile MD material; and (II) the high permittivity of the MD material ($\varepsilon' \approx 12$) can significantly degrade the antenna radiating properties. An MD substrate with a thickness of 5 mm is thus selected as a good tradeoff between the robustness and the desired antenna performance.

As regards the shorting wall, the ideal choice would have been a planar plate immersed in the MD material. This solution results in being impractical due to the fragile nature of the MD material: we thus adopt a curved shorting wall realized on the external face of the disk (see Figure 10a). The metallization for the antenna, the shorting plate and the ground plane is a 4 μm-thick silver film. The final antenna topology turns out to be the one reported in Figure 10a, where the position of the 50 Ω coaxial cable providing the best matching is also shown [9]. Figure 10b reports the simulated surface current at an operating frequency of 868 MHz: the expected behavior obeying the image theorem is obtained, corresponding to an almost zero current in the lower (radiating) edge and a maximum current in the upper (shorted) edge.

Figure 10. (**a**) Photo of the "button-shaped" patch antenna on a magneto-dielectric material. (**b**) Surface current distribution on patch metallization at 868 MHz.


| (a) | (b) |
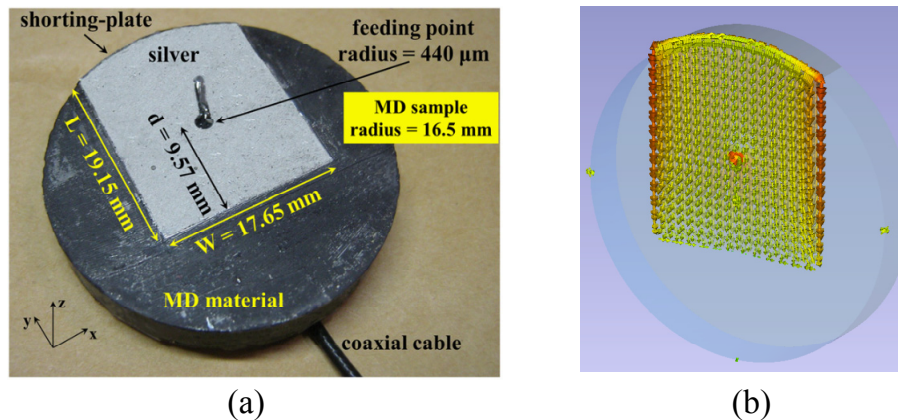
4.2. Results

The input port matching condition and the far-field performance of the realized prototype are compared with the corresponding full-wave simulation results in Figures 11 and 12, respectively.

The comparison of the reflection coefficient behaviors at the cable port of Figure 11 demonstrates the effectiveness of our design and of the MD material parameter characterization: the correspondence between measured and modelled results is excellent over a wide frequency band. In particular, the antenna operating bandwidth is significantly wider than standard patch antennas: a relative value of almost 29% is obtained by assuming as acceptable reflection in the limit of −10 dB. This positive behavior is mainly due to the high magnetic losses of the MD material (tan $\delta_\mu \approx 0.38$ at 868 MHz, from Table 1). These high losses represent the main drawback of the realized antenna: the simulated efficiency is equal to 1.5%, only. However, this low value is typical of electrically small antennas.

An improvement of the material synthesis procedure from the losses point of view will be a strategic issue in our future research.

Figure 11. (**a**) Measured and simulated reflection coefficient at the magneto-dielectric (MD)-antenna port. (**b**) Reflection coefficient of an only-dielectric (OD)-antenna with an identical refractive index, by varying the coaxial cable position.

(a)　　　　　　　(b)
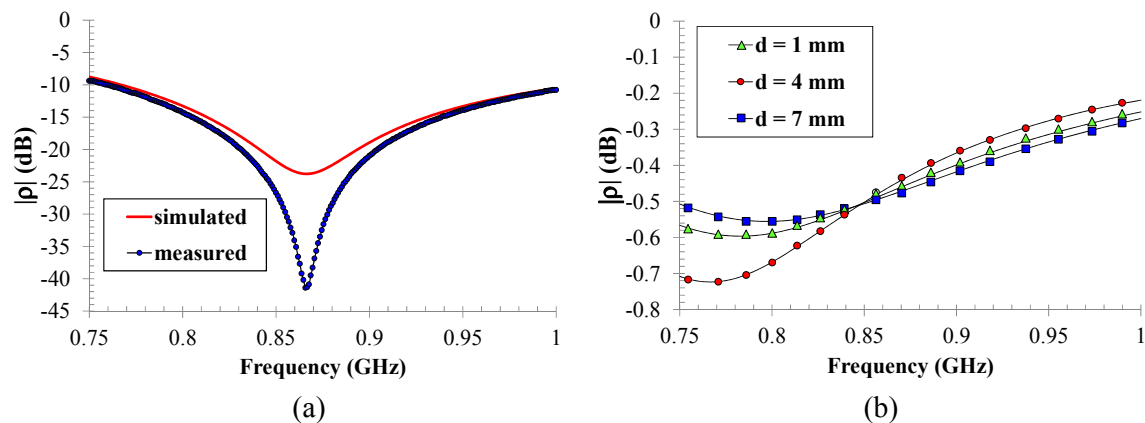
The Figure 11b underlines the advantage in using our MD material instead of an only-dielectric (OD) one, equivalent from the refractive index point of view. Here, the simulated reflection coefficient behavior of an identical patch built on a high-permittivity dielectric is given, for different feeding point positions. The high permittivity OD antenna cannot be matched to the 50 Ω feeding cable.

As regards the radiation performance, we exploit the foreseen wearable application of our button-shaped antenna by extending its ground plane. The first worn antenna measurement is carried out with a 10×10 cm^2 Global EMC-shielding fabric (the same used in the design of Section 3) behind the antenna prototype. This way, the broadside behavior of the antenna is preserved, as reported in Figure 12 for both the E- and H-plane of the antenna. Again, an excellent agreement between measurements and EM results is achieved, and this is true, both for simulation with and without background human tissue.

Figure 12. (**a**) E-plane and (**b**) H-plane normalized radiation patterns of the proposed MD-antenna at 868 MHz, on a conductive fabric and on a body.

(a)　　　　　　　(b)
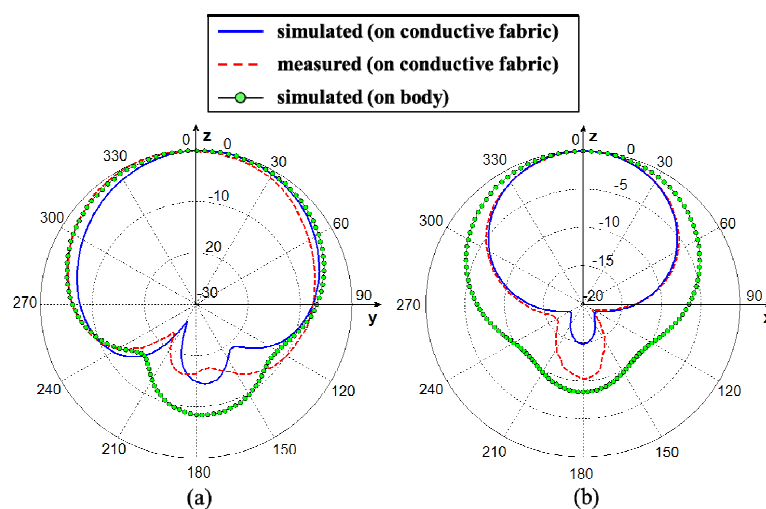
The same figure also shows the interesting simulated result of the worn antenna without the back-mounted shield: the skin itself acts as an extended ground plane, thus maintaining the desired broadside radiation behavior; the (computed) directivity is only 1.5 dBi lower with respect to the case with the extended fabric ground plane, and the front-to-back ratio is reduced to 8 dB, but still compatible with wearable applications.

5. Conclusions

We have presented some promising solutions for truly wearable and energy-autonomous systems using non-conventional materials. First, to obtain successful design results, the EM characteristics of these materials need to be established with respect to the operating frequency band. A robust procedure, making use of EM theory, full-wave numerical analysis and measurements has been demonstrated, both for dielectric fabrics and for conductive fabrics used in place of traditional planar metallization. A more complex procedure was needed to characterize dielectric and magnetic losses in the case of magneto-dielectric materials. Then, a rigorous nonlinear circuit technique has been described, including EM simulations, in order to accurately account for the actual layout of the compact wearable RF transceivers design. The accuracy in the optimization process is essential, especially when extremely low power budgets are involved. The integrated CAD approach here described combines all of these requisites, and its effectiveness is demonstrated in the design and measurement of two original radiating subsystems: a fully-wearable tri-band rectenna harvesting RF energy from humanized environments (covering the GSM and WiFi frequency bands) and a $\lambda_0/20$ UHF patch antenna on a new MD material. The conductive and non-conductive fabrics deployed in the rectenna projects reveal excellent performance, comparable with traditional RF circuit materials. The synthesized MD substrate for the PIFA operating at 868 MHz justifies the promising exploitation of materials with relative permeability greater than unity for miniaturization purposes: future improvements in the MD material synthesis process, mainly from the magnetic losses viewpoint, pave the way for a new generation of electrically small and efficient antennas.

Author Contributions

This paper is a review of the research activity of Alessandra Costanzo, Diego Masotti and Martino Aldrigo on wearable antennas. The three authors read and approved the final manuscript.

Conflicts of Interest

The authors declare no conflict of interest.

References

1. Rogier, H.; Agneessens, S.; Dierck, A.; Spinnewyn, B.; Stockman, G.-J.; Declercq, F.; van Torre, P.; Vallozzi, L.; vande Ginste, D. Active textile antennas in professional garments for sensing, localisation and communication. In Proceedings of the 2013 European on Microwave Conference (EuMC), Nuremberg, Germany, 6–10 October 2013; pp. 850–853.

2. Rizzoli, V.; Costanzo, A.; Masotti, D.; Lipparini, A.; Mastri, F. Computer-aided optimization of nonlinear microwave circuits with the aid of electromagnetic simulation. *IEEE Trans. Microw. Theory Tech.* **2004**, *52*, 362–377.

3. Rizzoli, V. Resonance Measurement of Single- and Coupled-Microstrip Propagation Constants. *IEEE Trans. MTT* **1977**, *25*, 113–120.

4. Lätti, K.-P.; Kettunen, M.; Ström, J.-P.; Silventoinen, P. A Review of Microstrip T-Resonator Method in Determining the Dielectric Properties of Printed Circuit Board Materials. *IEEE Trans. Instrum. Meas.* **2007**, *56*, 1845–1850.

5. Rashidian, A.; Aligodarz, M.T.; Klymyshyn, D.M. Dielectric characterization of materials using a modified microstrip ring resonator technique. *IEEE Trans. Dielectr. Electri. Insulation* **2012**, *19*, 1392–1399.

6. Costanzo, A.; Romani, A.; Masotti, D.; Arbizzani, N.; Rizzoli, V. RF/baseband co-design of switching receivers for multiband microwave energy harvesting. *Sens. Actuators A Phys.* **2012**, *179*, 158–168.

7. Masotti, D.; Costanzo, A.; Adami, S. Design and Realization of a Wearable Multi-Frequency Rf Energy Harvesting System. In Proceedings of the 5th European Conference on Antennas and Propagation (EuCAP), Rome, Italy, 11–15 April 2011; pp. 517–520.

8. Costanzo, A.; Masotti, D.; Donzelli, F.; Adami, S. Device to Convert Radiofrequency Electromagnetic Energy. Patent WO/2012/042348, PCT/IB2011/002253, 5 April 2012.

9. Aldrigo, M.; Costanzo, A.; Masotti, D.; Galassi, C. Exploitation of a novel magneto-dielectric substrate for miniaturization of wearable UHF antennas. *Mater. Lett.* **2012**, *87*, 127–130.

10. Declercq, F.; Couckuyt, I.; Rogier, H.; Dhaene, T. Environmental High Frequency Characterization of Fabrics Based on a Novel Surrogate Modelling Antenna Technique. *IEEE Trans. Antennas Propag.* **2013**, *61*, 5200–5213.

11. Hertleer, C.; van Laere, A.; Rogier, H.; van Langenhove, L. Influence of Relative Humidity on Textile Antenna Performance. *Text. Res. J.* **2010**, *80*, 177–183.

12. Lilja, J.; Salonen, P.; Kaija, T.; de Maagt, P. Design and Manufacturing of Robust Textile Antennas for Harsh Environments. *IEEE Trans. Antennas Propag.* **2012**, *60*, 4130–4140.

13. Bai, Q.; Langley, R. Crumpling of PIFA textile antenna. *IEEE Trans. Antennas Propag.* **2012**, *60*, 63–70.

14. Lilja, J.; Pynttari, V.; Kaija, T.; Makinen, R.; Halonen, E.; Sillanpaa, H.; Heikkinen, J.; Mantysalo, M.; Salonen, P.; de Maagt, P. Body-Worn Antennas Making a Splash: Lifejacket-Integrated Antennas for Global Search and Rescue Satellite System. *IEEE Antennas Propag. Mag.* **2013**, *55*, 324–341.

15. CST Microwave Studio 2012. Available online: http://www.cst.com (accessed on 1 January 2013).

16. Masotti, D.; Costanzo, A.; del Prete, M.; Rizzoli, V. A Genetic-Based Design of a Tetra-Band High-Efficiency RF Energy Harvesting System. *IET Microw. Antennas Propag.* **2013**, *7*, 1254–1263.

17. Hagerty, J.A.; Helmbrecht, F.B.; McCalpin, W.H.; Zane, R.; Popovic, Z.B. Recycling ambient microwave energy with broad-band rectenna arrays. *IEEE Trans. MTT* **2004**, *52*, 1014–1024.

18. Pinuela, M.; Yates, D.C.; Mitcheson, P.D.; Lucyszyn, S. London RF survey for radiative ambient RF energy harvesters and efficient DC-load inductive power transfer. In Proceedings of the 7th European Conference on Antennas and Propagation (EuCAP), Gothenburg, Sweden, 8–12 April 2013; pp. 2839–2843.

19. Visser, H.J.; Vullers, R.J.M. Wireless sensors remotely powered by RF energy. In Proceedings of the 6th European Conference on Antennas and Propagation (EuCAP), Prague, Czech Republic, 26–30 March 2012; pp. 1–4.

20. Monti, G.; Corchia, L.; Tarricone, L. UHF Wearable Rectenna on Textile Materials. *IEEE Trans. Antennas Propag.* **2013**, *61*, 3869–3873.

21. Rizzoli, V.; Costanzo, A.; Monti, G. General electromagnetic compatibility analysis for nonlinear microwave integrated circuits. *IEEE MTT-S Int. Microw. Symp. Dig.* **2004**, 953–956.

22. Georgiadis, A.; Andia, G.; Collado, A. Rectenna Design and Optimization Using Reciprocity Theory and Harmonic Balance Analysis for Electromagnetic (EM) Energy Harvesting. *IEEE Ant. Wirel. Prop. Lett.* **2010**, *9*, 444–446.

23. Love, A.E.H. The integration of equations of propagation of electric waves. *Trans. R. Soc. Lond.* **1901**, *197*, 1–45.

24. Chew, W.C. A Broad-Band Annular-Ring Microstrip Antenna. *IEEE Trans. Antennas Propag.* **1982**, *30*, 918–922.

25. Essel, J.; Brenk, D.; Heidrich, J.; Weigel, R. A Highly Efficient UHF RFID Frontend Approach. In Proceeding of the IEEE MTT-S International Microwave Workshop Wireless Sensing Local Positioning and RFID, Cavtat, Croatia, 24–25 September 2009; pp. 1–4.

26. Rizzoli, V.; Costanzo, A.; Masotti, D.; Aldrigo, M.; Donzelli, F.; Degli Esposti, V. Integration of nonlinear, radiation, and propagation CAD techniques for MIMO link design. *Int. J. Microw. Wirel. Technol.* **2012**, *4*, 223–232.

27. Waterhouse, R.B.; Targonski, S.D.; Kokotoff, D.M. Design and performance of small printed antennas. *IEEE Trans. Antennas Propag.* **1998**, *46*, 1629–1633.

28. Jungsuek, O.; Sarabandi, K.A. A Topology-Based Miniaturization of Circularly Polarized Patch Antennas. *IEEE Trans. Antennas Propag.* **2013**, *61*, 1422–1426.

29. Ikonen, R.; Rozanov, P.M.T.; Osipov, K.N.; Alitalo, A.V.; Tretyakov, S.A. Magnetodielectric Substrates in Antenna Miniaturization: Potential and Limitations. *IEEE Trans. Antennas Propag.* **2006**, *54*, 3391–3399.

30. Pereira, F.M.M.; Santos, M.R.P.; Sohn, R.S.T.M.; Almeida, J.S.; Medeiros, A.M.L.; Costa, M.M.; Sombra, A.S.B. Magnetic and dielectric properties of the M-type barium-strontium hexaferrite (BaxSr12xFe12O19) in the RF microwave (MW) frequency range. *J. Mater. Sci. Mater. Electron.* **2009**, *20*, 408–417.

31. Chen, H.-M.; Lin, Y.-F. Experimental and simulated studies of planar inverted-F antenna. In Proceedings of the IEEE International Workshop on Antenna Technology: Small Antennas and Novel Metamaterials, Singapore, 7–9 March 2005; pp. 299–302.